



This is a repository copy of *Soft-magnetic behaviour of Fe-based nanocrystalline alloys produced using laser powder bed fusion*.

White Rose Research Online URL for this paper:

<https://eprints.whiterose.ac.uk/202022/>

Version: Published Version

---

**Article:**

Ozden, M.G., Freeman, F.S.H.B. [orcid.org/0000-0002-7402-1790](https://orcid.org/0000-0002-7402-1790) and Morley, N.A. (2023) Soft-magnetic behaviour of Fe-based nanocrystalline alloys produced using laser powder bed fusion. *Advanced Engineering Materials*. 2300597. ISSN 1438-1656

<https://doi.org/10.1002/adem.202300597>

---

**Reuse**

This article is distributed under the terms of the Creative Commons Attribution-NonCommercial-NoDerivs (CC BY-NC-ND) licence. This licence only allows you to download this work and share it with others as long as you credit the authors, but you can't change the article in any way or use it commercially. More information and the full terms of the licence here: <https://creativecommons.org/licenses/>

**Takedown**

If you consider content in White Rose Research Online to be in breach of UK law, please notify us by emailing [eprints@whiterose.ac.uk](mailto:eprints@whiterose.ac.uk) including the URL of the record and the reason for the withdrawal request.



[eprints@whiterose.ac.uk](mailto:eprints@whiterose.ac.uk)  
<https://eprints.whiterose.ac.uk/>

# Soft-Magnetic Behavior of Fe-Based Nanocrystalline Alloys Produced Using Laser Powder Bed Fusion

Merve G. Özden,\* Felicity SHB Freeman, and Nicola A. Morley

Herein, an extensive experimental study is presented on the influence of the major process parameters of the laser powder bed fusion (LPBF) technique on the bulk density and soft-magnetic properties of Fe-based bulk metallic glasses (BMGs). For this purpose, 81 samples are manufactured using the combinations of different process parameters, that is, layer thickness ( $t$ : 50–70  $\mu\text{m}$ ), laser power ( $P$ : 70–130 W), laser scan speed ( $v$ : 900–1100  $\text{mm s}^{-1}$ ), and hatch spacing ( $h$ : 20–40  $\mu\text{m}$ ). High bulk density ( $\geq 99\%$ ) is achieved utilizing low  $P$  and  $v$  combined with low  $h$  and  $t$  in order to decrease energy input to the powder, preventing cracks associated with the brittle nature of BMGs. Furthermore, it is indicated that  $h = 30 \mu\text{m}$  and  $v = 1000 \text{mm s}^{-1}$  play a determining role in acquiring high saturation magnetization ( $\geq 200 \text{Am}^2 \text{kg}^{-1}$ ). Due to the laser scanning nature of the process, two distinct microstructures evolve, melt-pool (MP) and heat-affected zone (HAZ). According to thermal modeling performed in this study, laser power has the major effect on the thermal development in the microstructure (thermal gradient evolved between the two hatches and the cooling rate from MP through HAZ).

electromagnetic systems to increase their efficiency by lowering the energy losses considerably for eddy currents.<sup>[3]</sup> Recently, Thorsson et al. managed to produce a Fe-based nanocrystalline complex-shaped electric motor rotor with a 6 cm diameter by selective laser melting,<sup>[4]</sup> enabling its users to build 3D complicated shapes in one-production step without the need of postprocessing.<sup>[5]</sup> The 3D-printed electric motor rotor possessed high electrical resistivity (178.2  $\mu\Omega \text{cm}$ ), high magnetic susceptibility (9.17), relatively high saturation magnetization (1.29 T), and relatively small coercivity (0.51  $\text{kA m}^{-1}$ ), which are the key factors for electric motors. Moreover, the electric motor rotor was fabricated with much larger than critical casting thickness (6 cm) due to the high cooling rate evolving in the whole part.<sup>[4]</sup> This can only be achieved by using laser additive manufacturing (LAM).

Laser powder bed fusion (LPBF), as one of the LAM techniques, has been


exploited widely for Fe-based amorphous/nanocrystalline ferromagnetic materials. LPBF, also known as selective laser melting (SLM), manufactures dense metallic components in a layer-by-layer fashion by using a focused laser beam, scanning each powder layer.<sup>[6]</sup> Figure 2a shows the main process parameters of LPBF technique. Optimization of those parameters plays an important role in producing Fe-based amorphous/nanocrystalline alloys as changing parameters affect the microstructural evolution, which is complex and heterogeneous, as shown in Figure 2b. Because of the laser scanning nature of the LPBF process, the microstructure usually contains two distinct regions, melt pool (MP) and heat-affected zones (HAZ), both of which experience different cooling rates.<sup>[7]</sup> One of the main challenges in LPBF technique is process optimization to control the microstructure of Fe-based amorphous/nanocrystalline ferromagnets to enhance their soft-magnetic properties.

This article addresses this issue to comprehend how microstructural development influences the magnetic properties of Fe-based alloys as well as how bulk density changes with different process parameters. To do this, all the major process parameters were considered: laser power ( $P$ ), laser scan speed ( $v$ ), hatch spacing ( $h$ ), and layer thickness ( $t$ ). Researchers have generally investigated the effects of laser power and laser scan speed on the properties of Fe-based MG.<sup>[3,8–11]</sup> This work provides a comprehensive experimental study to optimize the LPBF process for the differing process parameters ( $P$ ,  $v$ ,  $h$ , and  $t$ ).

## 1. Introduction

Ferromagnetic metallic glasses (MGs) have been studied extensively owing to their lack of crystalline defects, resulting in superior soft-magnetic properties. Crystalline-related imperfections lead to magnetic anisotropy, which in turn increases the coercive field within the material. Thus, low coercivity is achieved with a fully amorphous phase present in the material.<sup>[1]</sup> Introducing nanocrystalline phases into an amorphous matrix provides higher saturation magnetization and higher permeability (Figure 1), especially in Fe-based ferromagnets.<sup>[2]</sup> Their exceptional soft-magnetic properties allow them to be utilized as a magnetic core material in

M. G. Özden, F. B. Freeman, N. A. Morley  
Department of Material Science and Engineering  
University of Sheffield  
Sheffield S1 3JD, UK  
E-mail: mgozden1@sheffield.ac.uk

 The ORCID identification number(s) for the author(s) of this article can be found under <https://doi.org/10.1002/adem.202300597>.

© 2023 The Authors. Advanced Engineering Materials published by Wiley-VCH GmbH. This is an open access article under the terms of the Creative Commons Attribution-NonCommercial-NoDerivs License, which permits use and distribution in any medium, provided the original work is properly cited, the use is non-commercial and no modifications or adaptations are made.

DOI: 10.1002/adem.202300597

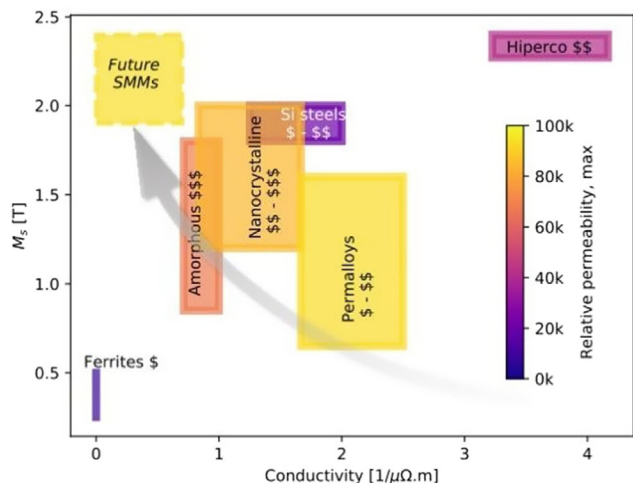


**Figure 1.** Relative permeability, conductivity, and saturation magnetization of soft-magnetic materials, where the color shading represents the relative permeability and the \$ represents the relative cost of the material.

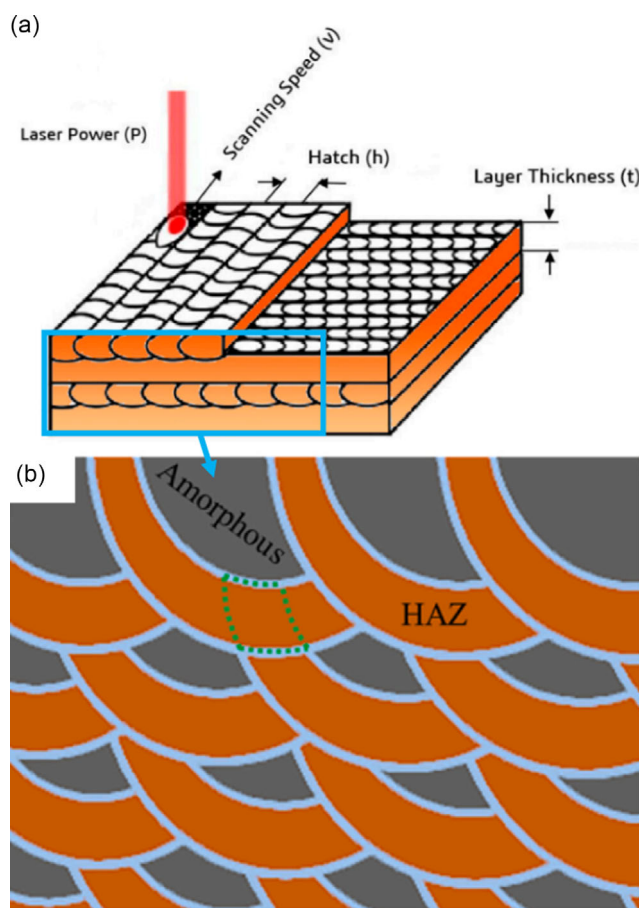


**Figure 2.** a) The studied process parameters of LPBF technique (Reproduced under terms of the CC-BY license.<sup>[28]</sup> 2019 by the authors, published by MDPI) and b) the schematic illustrations of microstructural development of BMGs during LPBF process (Reproduced with permission.<sup>[29]</sup> 2022, Elsevier).

## 2. Experimental Section

### 2.1. Material

The amorphous ferromagnetic powder (KUAMET 6B2 ( $\text{Fe}_{87.38}\text{Si}_{6.85}\text{B}_{2.54}\text{Cr}_{2.46}\text{C}_{0.77}$  (mass %))), provided by Epson Atmix Corporation, Japan, was chosen for this study. This was because the elements within the Fe–Si–B–Cr–C system are widely available and more sustainable than its competitive materials, containing Co or rare earth materials such as Nd and Dy. The only expensive element in the alloy is boron, however, with a smaller quantity (2.54%) compared to other amorphous alloys. The powder characterization results can be found in our previous work.<sup>[12]</sup> According to the results, the amorphous spherical powder has a narrow particle size distribution with D10, D50, and D90 of 9.49, 23.4, and 47.5  $\mu\text{m}$ , respectively. In addition, it shows soft-magnetic behavior with saturation magnetization of 102  $\text{Am}^2\text{kg}^{-1}$  and coercivity of 2.27  $\text{kA m}^{-1}$ .

### 2.2. Methods

First, powder sieving was carried out using a 53  $\mu\text{m}$  mesh-size sieve to narrow the particle size distribution down for better spreadability and flowability over the powder bed. An Aconity Mini machine was used to print the cylindrical samples with the dimensions of 6 mm in diameter and 5 mm in height. Different combinations of process parameters were applied to study their individual effect on the properties (Appendix A). For all layer thicknesses,  $t$  (50, 60, and 70  $\mu\text{m}$ ), same hatch spacing,  $h$  (20, 30, and 40  $\mu\text{m}$ ), and laser scan speed,  $v$  (900, 1,000, 1,100  $\text{mm s}^{-1}$ ) values were maintained, however, with the increasing layer thickness, it was necessary to increase laser power to obtain bulk dense parts, as stated in our previous work.<sup>[12]</sup> Therefore, at  $t = 50 \mu\text{m}$ ,  $P = 70, 80,$  and  $90 \text{ W}$  (Table A1); at  $t = 60 \mu\text{m}$ ,  $P = 90, 100, 110 \text{ W}$  (Table A2) and at  $t = 70 \mu\text{m}$ ,  $P = 110, 120,$  and  $130 \text{ W}$  (Table A3) were used. All the samples were printed using the hatch filling type with a starting angle of 22.5° and rotation of 70° after each layer and the residual oxygen content of the chamber was kept below 0.01% to prevent oxidation.

The 3D melt pool modeling was carried out in MATLAB using the Eagar solution for a moving Gaussian heat source.<sup>[13]</sup> The modeling provides the cooling rate, thermal gradient, melt-pool (MP) width, length, and depth at given process conditions and material's properties. After the production of the samples, their densities were measured with an Archimedes technique set-up three times. The bulk density percentage was quantified using the mean density and the theoretical density ( $7.294 \text{ gr cm}^{-3}$ ) for every sample, this also gave the porosity as well. Moreover, the micrographs of the samples were taken by INSPECT F50 HR-SEM after they were ground, polished, and subjected to etching for 3 min with 2% nital solution (98 mL  $\text{HNO}_3$  and 2 mL ethanol). The crystallite sizes were calculated from those micrographs using the ImageJ program. Differential scanning calorimetry (DSC) (TA instruments SDT Q600 machine) was utilized by heating the samples with a rate of 20  $^\circ\text{C min}^{-1}$  up to 1,400  $^\circ\text{C}$  to obtain their crystallization enthalpies. Then, the amorphous content was quantified by using the technique, described in these articles.<sup>[3,10,14]</sup> Finally, the magnetic properties (saturation magnetization and coercivity) were determined from magnetization

hysteresis (M–H) loops, which were obtained using a SQUID magnetometer MPMS3 from Quantum Design at 300 K and fields up to  $160 \text{ kA m}^{-1}$ .

### 3. Results and Discussion

As stated in our previous work,<sup>[12]</sup> due to the high thermal gradients ( $5.67 - 11.9 \times 10^6 \text{ K m}^{-1}$ ) evolved between the two hatches, the cooling rate ( $5.1 - 12.9 \times 10^6 \text{ K s}^{-1}$ ) significantly differs so that four phases develop in the distance of hatch spacing (Figure 3). The  $\alpha\text{-Fe(Si)}$  phase mainly evolves in the melt pool (MP) region (Figure 3a,b) whereas  $\text{Fe}_3\text{Si}$  nanoclusters and  $\text{Fe}_2\text{B}$  crystallites exist in the heat-affected zone (HAZ) region (Figure 3f). In the HAZ region, the presence of the ordered  $\text{Fe}_2\text{B}$  phase implies that within the HAZ a thermal equilibrium

condition (slower cooling rate) has been reached. Phase identification (XRD, TEM, and DSC analysis) was performed in the previous study,<sup>[12]</sup> where it was shown that the disordered  $\alpha\text{-Fe(Si)}$ , the ordered  $\text{Fe}_3\text{Si}$ , and the stable  $\text{Fe}_2\text{B}$  phases grow as equiaxed, dendritic (star-like), and needle-like, respectively. Moreover, the size of the  $\alpha\text{-Fe(Si)}$  phase increases from the MP to the end of HAZ region (Figure 3a,b), which means this phase has a variety of crystallite sizes within the same MP region. For this reason, its grain size was represented for the particle size distribution in the form of histogram graph in this study, where the effect of process parameters on the particle size distribution of the  $\alpha\text{-Fe(Si)}$  phase was investigated. The cooling rate mostly influences the amorphous content and grain size in the MP region, which in turn affects the soft-magnetic properties.

Despite the high cooling rates within the process, there was a smaller amount of the amorphous phase content ( $\leq 30\%$ ) within

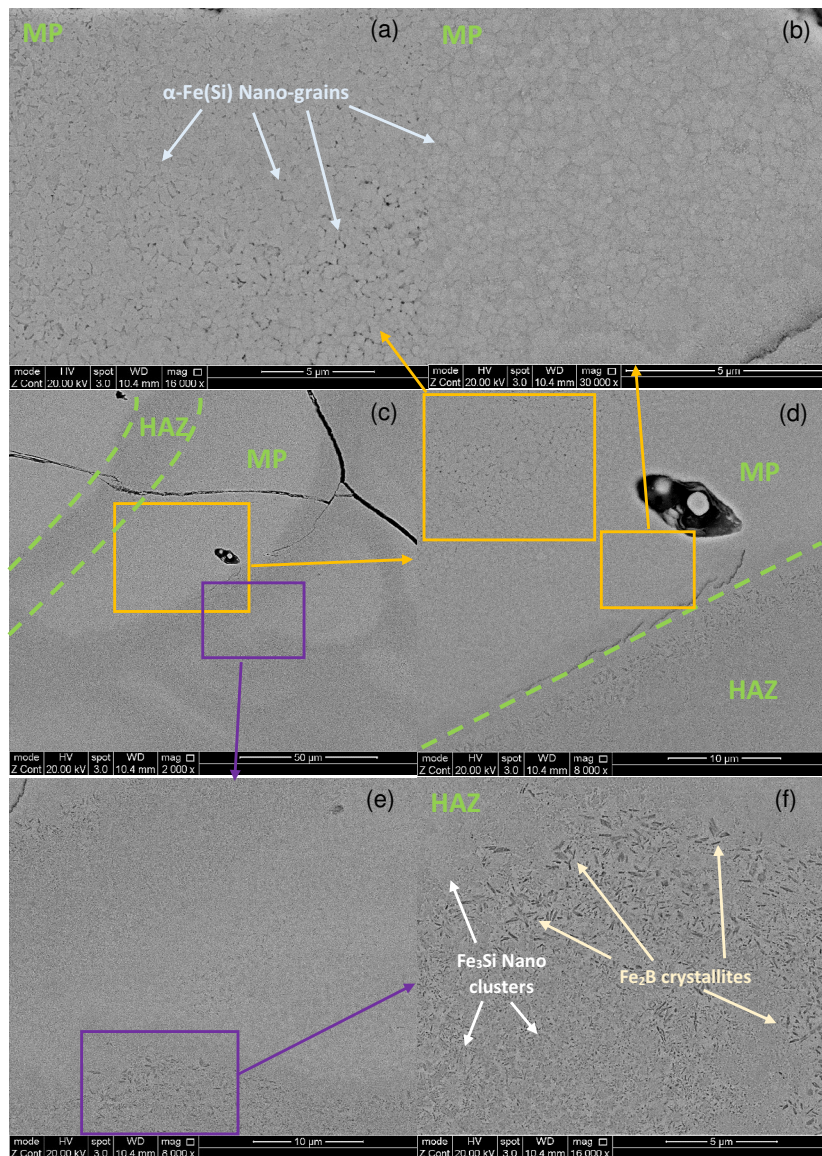


**Figure 3.** SEM micrographs of LPBF processed samples showing a,b) the microstructures in melt pool zone (MP) containing  $\alpha\text{-Fe(Si)}$  grains; c,d) MP and HAZ regions at higher magnification; e,f) the microstructures in the heat-affected zone (HAZ) composed of  $\text{Fe}_3\text{Si}$  and  $\text{Fe}_2\text{B}$  nanophases.

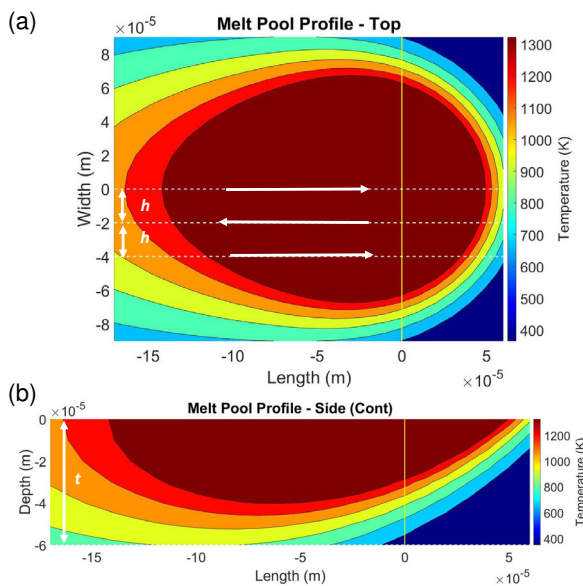


**Figure 4.** 3D melt-pool modeling of a) top view and b) side (cross-sectional view) of LPBF processed samples with  $P$  of 100 W,  $v$  of 900 mm s<sup>-1</sup>,  $h$  of 20  $\mu$ m and  $t$  of 60  $\mu$ m, showing temperature profile in melt-pool region ( $h$  is hatch spacing and  $t$  is layer thickness). It should be noted that the dark red region symbolizes a fully liquid melt-pool whereas lighter red areas depict a mushy zone (liquid and solid together).

the samples, than was expected. The reasons for this may be due to 1) defects in the microstructure (cracks and pores) that facilitate the heterogeneous nucleation of crystalline phases and 2) in situ heat treatment evolved resulting from previous hatches. In **Figure 4a**, white arrows represent the hatches and their directions show the laser scanning route. It can be seen from this figure that when the hatch spacing is low (20  $\mu$ m), the laser scan re-heats the previously-solidified regions, which gives an in situ heat treatment that is above the crystallization temperature ( $\approx$ 800 K). In addition, due to the too small sample size (6 mm), previous hatches may not have fully cooled down when the subsequent hatch was being laser-scanned. This multiple reheating decreased the cooling rate, which promote nucleation. Furthermore, this rescanning helped to improve bulk density (98.18%) as at the layer thickness of 60  $\mu$ m, MP depth was 40  $\mu$ m (**Figure 4b**), which was not enough to solidify all the powders. Without the multiple laser scanning, this would give rise to a lack within the samples.

The modeling gives the cooling rate, thermal gradient from the MP through the HAZ and the MP dimensions (width-length (area) and depth) for the given process parameters. It was found that layer thickness ( $t$ ) and hatch spacing ( $h$ ) did not have a noteworthy impact on those thermal conditions. In contrast, the main effect on the thermal evolution during the LPBF process was the laser power. In general, it was observed that increasing  $P$  makes the MP bigger (**Figure 5c,d**), which results in a slower solidification (**Figure 5a**). Additionally, the modeling suggested that the

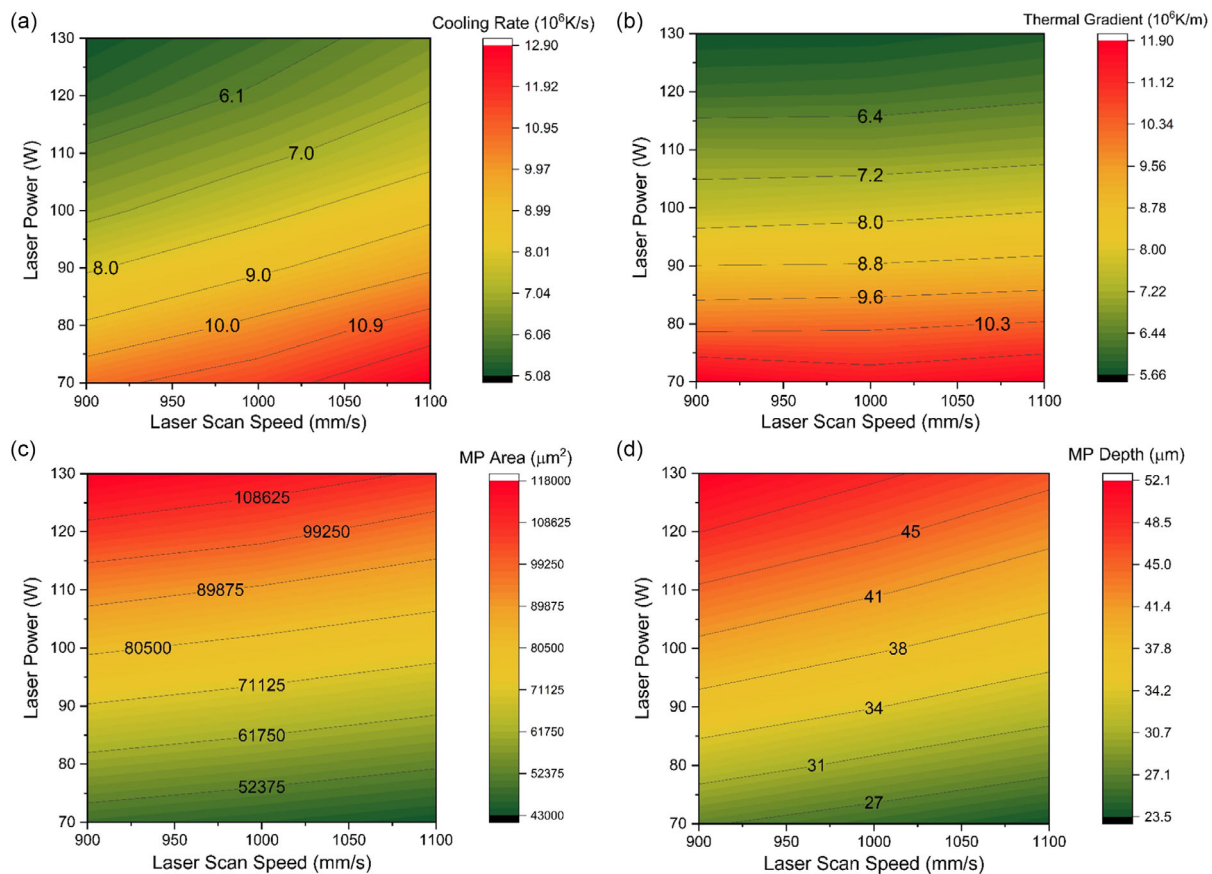


**Figure 5.** The color-map graphs of a) the cooling rate, b) thermal gradient, c) melt-pool (MP) area, and d) melt-pool depth as a function of laser power and laser scan speed.

thermal gradient is only influenced by  $P$ . High thermal gradient and cooling rate can only be achieved at low  $P$  (Figure 5b). In addition to  $P$ , the laser scan speed ( $\nu$ ) also affected the cooling rate and MP depth, such that high  $\nu$  decreased the depth and increased the cooling rate.

Elemental analysis showed the Fe content in the samples is around 82 wt%. The only noteworthy differences between MP and HAZ regions are that the Fe content is higher in the MP (due to amorphous and  $\alpha$ -Fe phases) and the B content is higher in the HAZ region, because of  $\text{Fe}_2\text{B}$  phases (Table 1). While EDS gives the general idea about elemental compositions for comparison, it is worth mentioning that it is not reliable to investigate exact compositions resulting from the presence of B and C in the

**Table 1.** EDS results of the LPBF-processed samples and their MP and HAZ regions in their microstructure.

wt%	General	MP	HAZ
Fe	81.9 ± 0.4	83.0 ± 0.9	80.8 ± 0.8
Si	6.0 ± 0.1	6.1 ± 0.1	5.9 ± 0.1
B	3.1 ± 0.5	1.8 ± 1.0	3.9 ± 1.0
Cr	2.5 ± 0.1	2.6 ± 0.1	2.4 ± 0.1
C	6.5 ± 0.1	6.5 ± 0.2	7.0 ± 0.3

sample, as they are light elements, which are known to be difficult to quantify using EDS.<sup>[15]</sup>

Before starting to investigate the change in magnetic properties with different process parameters, it is worth noting that in general, the saturation magnetization,  $M_s$  is influenced dominantly by the amount of magnetic transition metals (Fe, Co, and Ni) present because of their high magnetic moments.<sup>[16]</sup> In literature, amorphous ferromagnets containing 82 wt% of Fe possess a saturation magnetization of  $180 \text{ Am}^2 \text{ kg}^{-1}$ <sup>[17]</sup> ( $1.6 \text{ T}^{[18,19]}$ ). Nevertheless, it was well-established that their saturation magnetization can be enhanced considerably by nucleating nanometer-sized phases in an amorphous matrix.<sup>[17–20]</sup> Meanwhile, the coercivity strongly depends on the grain size.<sup>[20]</sup> It was proven that the coercivity has the lowest value ( $\leq 10 \text{ A m}^{-1}$ ) for grain sizes ( $D$ ) that are either less than  $40 \text{ nm}$  or more than  $100 \mu\text{m}$ .<sup>[21,22]</sup> According to the theoretical predictions based on the random anisotropy model for the average magneto-crystalline anisotropy constant, the coercivity ( $H_c$ ) exhibits a decrease that follows the sixth power of the grain size ( $D^6$ ), from  $100 \text{ nm}$  down to the amorphous phase.<sup>[23]</sup> Between  $100 \text{ nm}$  and  $500 \text{ nm}$ , the coercivity is constant at values above  $1 \text{ kA m}^{-1}$ . At  $D \geq 500 \text{ nm}$ ,  $H_c$  has a dependence of  $1/D$ , which aligns with the conventional principle that achieving desirable soft magnetic properties typically necessitates the presence of significantly large grains ( $D > 100 \mu\text{m}$ ) in bulk samples. Consequently, when the

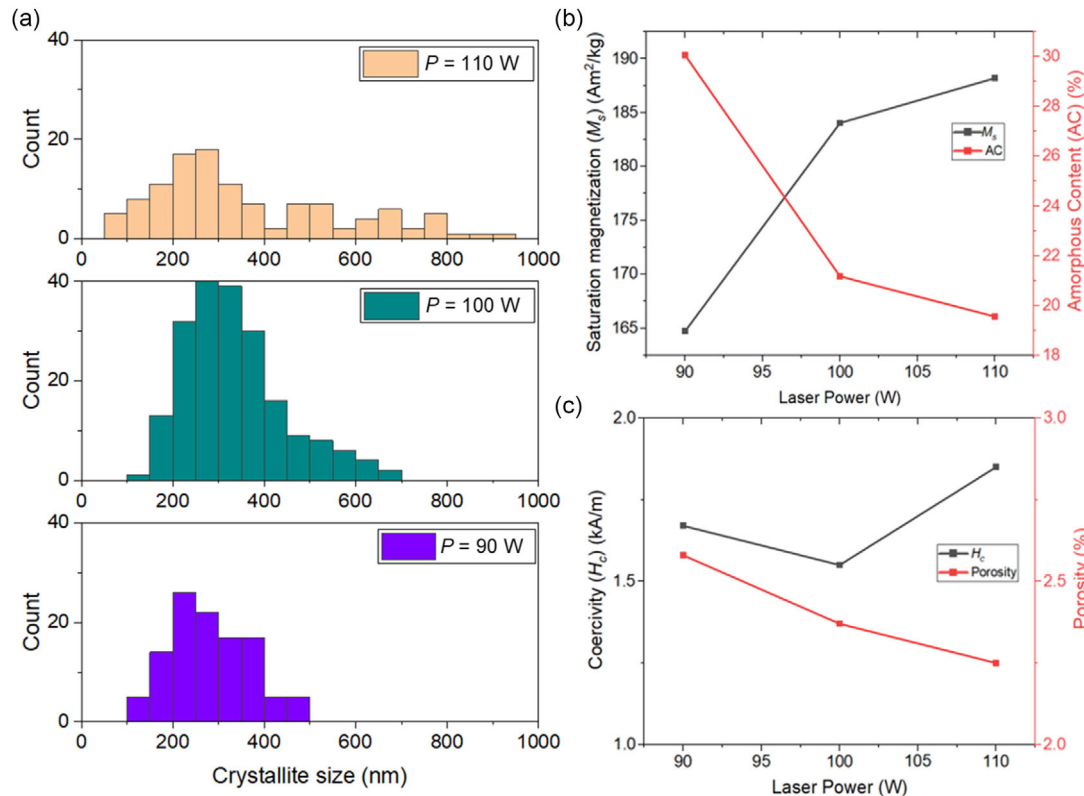


**Figure 6.** The characterization results demonstrate the effect of laser power on the microstructural and magnetic properties of 3D printed samples by using different laser power (90, 100, and 110 W) (other parameters kept constant;  $\nu = 900 \text{ mm s}^{-1}$ ,  $h = 30 \mu\text{m}$ ,  $t = 60 \mu\text{m}$ ): a) The histogram graphs showing  $\alpha$ -Fe(Si) crystallite size distribution and the graphs illustrating b) saturation magnetization and amorphous content, c) coercivity and porosity values as a function of laser power.

particle size is reduced to approach the width of the domain wall,  $H_c$  increases, reaching a maximum value determined by the existing anisotropies.<sup>[24]</sup> This means as the grain size increases, the magneto-crystalline anisotropy decreases on the macroscopic scale due to the reduction in the grain boundary area.  $\text{Fe}_2\text{B}$  tetragonal structure has much higher magneto-crystalline anisotropy (anisotropy constant ( $K_1$ :  $100 \text{ kJ m}^{-3}$ ) than bcc-Fe phase ( $K_1$ :  $8 \text{ kJ m}^{-3}$ )). Nevertheless, since the quantity of the  $\text{Fe}_2\text{B}$  phase is very small in the microstructure compared to the bcc-Fe phase and its size does not change considerably with different process parameters, its effect on coercivity was ignored in this study. However, to minimize the coercivity, one might consider preventing the formation of  $\text{Fe}_2\text{B}$  phase in the microstructure. The amorphous content also changes the magnetic properties, i.e., a higher content is expected to reduce the saturation magnetization ( $M_s$ ) and coercivity ( $H_c$ ).

Laser power ( $P$ ) is the most dominant parameter to vary the thermal profile in the microstructure. As mentioned before, laser power mainly affects the cooling rate and thermal gradient. The maximum nucleation rate occurs just above the glass transition temperature and lowers quickly with increasing temperature, whereas the growth rate continues to increase, reaching its maximum at much higher temperature.<sup>[25]</sup> For this reason, a higher cooling rate and thermal gradient (low  $P$ ) promote

nucleation while a lower cooling rate and thermal gradient (high  $P$ ) accelerate grain growth (grains are bigger in size, rather than increase in number). Increasing  $P$  from 90 to 100 W increases the nucleation rate, in contrast, at  $P = 110 \text{ W}$ , growth of the nucleus is dominant (Figure 6a). At low  $P$  ( $=90 \text{ W}$ ), there are a few smaller  $\alpha\text{-Fe}(\text{Si})$  grains (narrow particle size distribution) in the MP region (Figure 6a), which implies higher cooling rate, i.e., high amorphous content (Figure 6b). High  $M_s$  at high  $P$  may result from the low amorphous content or the increase in the size of bcc-Fe phase. Coercivity ( $H_c$ ) is affected by not only magnetic anisotropy associated with the grain size, but also defects in the parts (porosity and cracks). High coercivity at  $P = 110 \text{ W}$  may originate from the low amorphous content (Figure 6b), so a larger contribution from the magnetocrystalline anisotropy.

Laser scan speed ( $\nu$ ) impacts the time parameter in the cooling rate expression. Low  $\nu$  provides a longer time between laser scan tracks, lowering the cooling rate and increasing the crystallization rate at a constant temperature.<sup>[26]</sup> However, owing to the small effect of  $\nu$  on the cooling rate, the microstructure (the crystallite size distribution (Figure 7a) and amorphous content (Figure 7b)) does not vary significantly. The slight increase in  $M_s$  with decreasing  $\nu$  may be due to the lower amorphous content (Figure 7b). When other parameters are constant and moderate, increasing  $\nu$  brings about the balling effect (this phenomenon

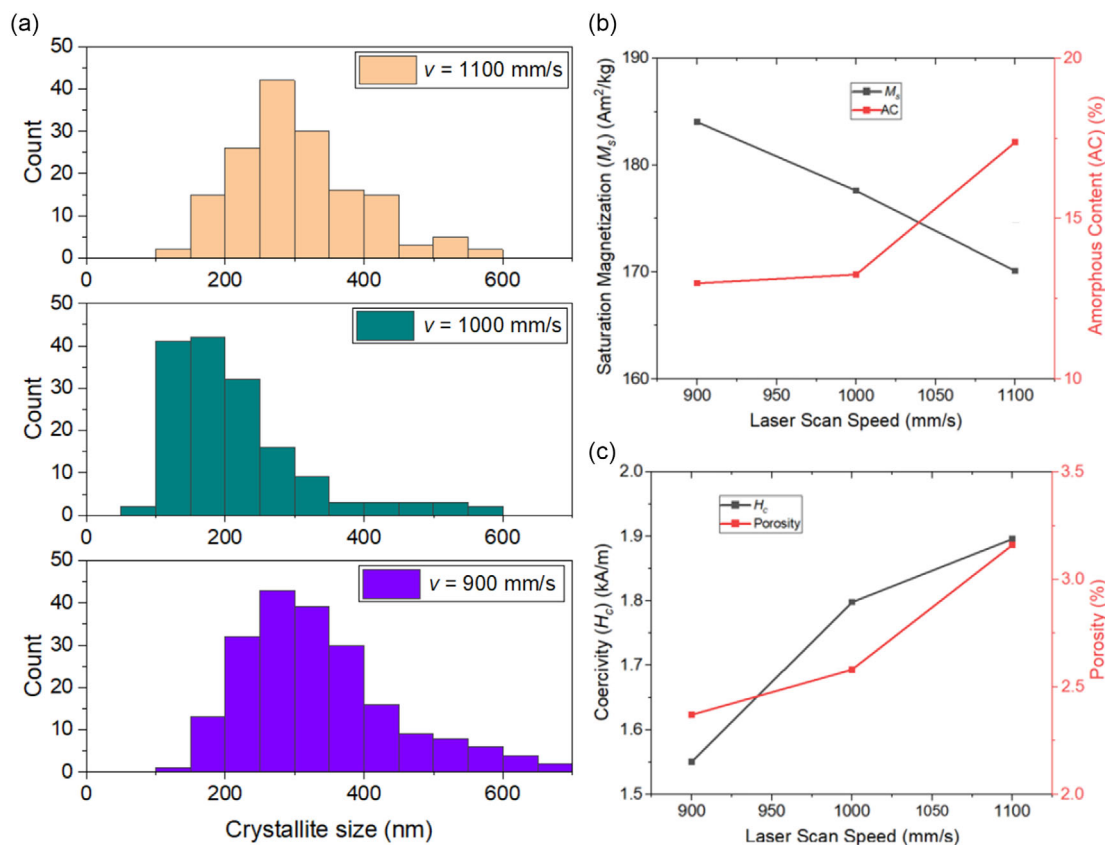


**Figure 7.** The characterization results demonstrate the effect of laser scan speed on the microstructural and magnetic properties of 3D printed samples by using different laser scan speeds (900, 1,000, and 1,100  $\text{mm s}^{-1}$ ) (other parameters kept constant;  $P = 100 \text{ mm s}^{-1}$ ,  $h = 30 \mu\text{m}$ ,  $t = 60 \mu\text{m}$ ): a) The histogram graphs showing  $\alpha\text{-Fe}(\text{Si})$  crystallite size distribution and the graphs illustrating b) saturation magnetization and amorphous content, c) coercivity and porosity values as a function of laser scan speed.

generally occurs at high  $\nu$  or large  $h$  due to unstable melt. More detailed information can be found elsewhere),<sup>[27]</sup> leading to higher porosity content. Even though the microstructure does not change considerably, high coercivity at high  $\nu$  ( $=1,100 \text{ mm s}^{-1}$ ) is observed, suggesting that the higher porosity level, i.e., lower bulk density, worsens the coercivity (Figure 7c).

Although hatch spacing ( $h$ ) and layer thickness ( $t$ ) do not influence notably the thermal development in the microstructure theoretically; in practice, shorter  $h$  can lead to reheating the already solidified part, depending on the MP size. This can bring about in situ heat treatment. This effect is even more weighty when the component size is small. In this study, because of the small sample size (6 mm in diameter), when the laser starts to scan the subsequent hatch, the previous hatch may not have cooled down completely. If the hatch spacing is too short (20 and 30  $\mu\text{m}$ ) considering the MP size (Figure 4a), the hatches experience multiple reheating, which lowers the cooling rate. This makes grain growth dominant over nucleation from the crystallization kinetics point of view. At low  $h$  (Figure 8a), the crystallite size increases in the MP, causing high  $M_s$  despite high amorphous content (Figure 8b). Although  $h$  does not have substantial effect on the coercivity, high  $h$  lowers the bulk density by 1% due to the balling effect (Figure 8c).

The statistical analysis performed based on the thermal modeling indicates that the layer thickness ( $t$ ) has the same effect

with  $P$  on the cooling rate, which means increasing  $t$  lowers the cooling rate. As a result, the sample processed with high  $t$  (70  $\mu\text{m}$ ) possesses larger  $\alpha\text{-Fe}$  crystallites (Figure 9a). Nevertheless, this did not alter the soft-magnetic behavior (high  $M_s$ , low  $H_c$ ) considerably (Figure 9b,c). Despite the slight change, the dependence of  $H_c$  on  $1/D$  can be observed in Figure 9.

While investigating the laser process parameters individually gives great insight into the thermal and crystallization characteristics of the LPBF process, this is not enough to achieve desirable properties. All of the major process parameters must be taken into account together since they are dependent on each other.

The graphs showing the bulk density variations as a function of laser scan speed and laser power at different hatch spacing and layer thickness are presented in Figure 10. If a bulk density of 97%, i.e., 3% porosity, is set to be a design limit for a given application, then the green and yellow regions demonstrate low density. In general, high laser power creates cracks due to the brittle nature of metallic glasses, especially at high laser power ( $\geq 120 \text{ W}$ ) and low hatch spacing ( $=20 \mu\text{m}$ ). In addition, the combination of laser scan speed ( $\nu$ ), hatch spacing ( $h$ ), and low laser power ( $P$ ) creates an extensive balling effect resulting from the small volumes of melt pools and large distances between them. This eventually leads to large metallurgical pores in the microstructure, decreasing the bulk density. However, low  $P$  brings about high bulk density

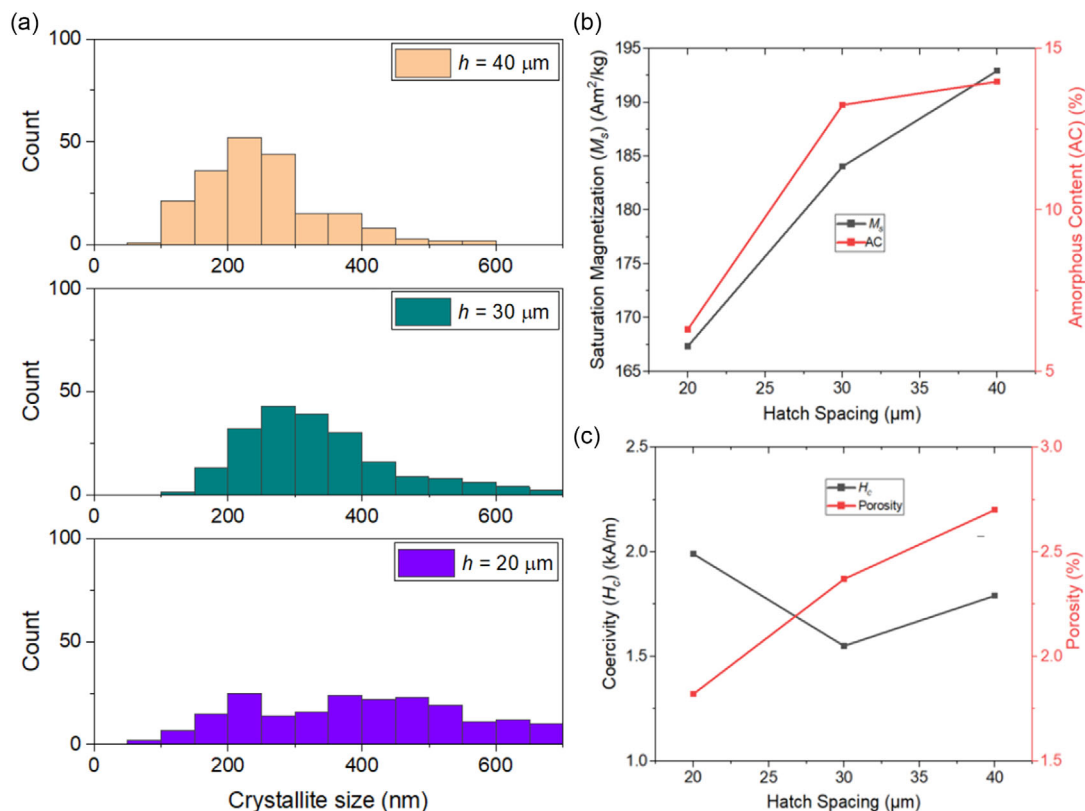


**Figure 8.** The characterization results demonstrate the effect of hatch spacing on the microstructural and magnetic properties of 3D-printed samples by using different hatch spacing (20, 30, and 40  $\mu\text{m}$ ) (other parameters kept constant;  $\nu = 900 \text{ mm s}^{-1}$ ,  $P = 100 \text{ W}$ ,  $t = 60 \mu\text{m}$ ): a) The histogram graphs showing  $\alpha\text{-Fe(Si)}$  crystallite size distribution and the graphs illustrating b) saturation magnetization and amorphous content, c) coercivity and porosity values as a function of hatch spacing.



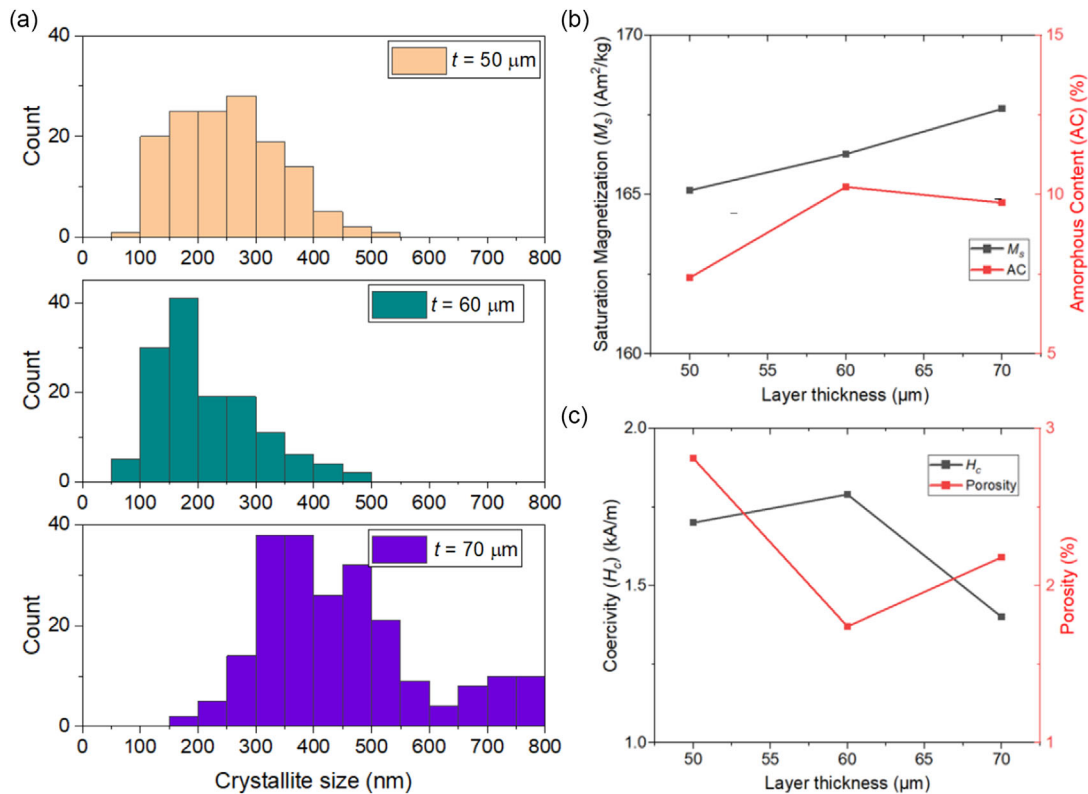


**Figure 9.** The characterization results demonstrate the effect of layer thickness on the microstructural and magnetic properties of 3D printed samples by using different layer thicknesses (50, 60, and 70  $\mu\text{m}$ ) (other parameters kept constant;  $v = 1000 \text{ mm s}^{-1}$ ,  $P = 90 \text{ W}$ ,  $h = 20 \mu\text{m}$ ): a) The histogram graphs showing  $\alpha\text{-Fe(Si)}$  crystallite size distribution and the graphs illustrating b) saturation magnetization and amorphous content, c) coercivity and porosity values as a function of layer thickness.

(red regions) when it is used with low  $v$ ,  $h$ . As stated before, high  $v$  ( $1,100 \text{ mm s}^{-1}$ ) and low  $P$ , especially along with high  $h$  ( $40 \mu\text{m}$ ), provide high cooling rate, leading to high internal thermal stresses generating cracks. They are generally formed around micropores acting as thermal stress concentrations. Also, the combination of high  $v$  and low  $P$  does not give enough heat input to the powder, resulting in incomplete melting and interparticle bonding. This increases porosity. Nevertheless, rapid cooling rate (low  $P$  and high  $v$ ) is a necessity for the development of the amorphous phase. Thus, to increase the amorphous content as well as bulk density (i.e., reduce porosity), one should consider thermal annealing as a postprocess to get rid of the internal stresses or double scanning (in situ heat treatment). It should contain the first scan with high  $E$  ( $=P/(vth)$ ) to improve sintering and a second scan with low  $E$  to increase amorphous content.

When the process parameters were investigated individually, it was observed that as  $P$ ,  $t$ , and  $h$  were increased and  $v$  was decreased,  $M_s$  values were enhanced. When the different combinations of process parameters were examined (Figure 11), conflicting results were obtained as the process parameters are intercorrelated with each other. The most distinguishable difference is that at high  $h$ ,  $M_s$  worsens. Previously, it was mentioned that increasing  $h$  (at  $P = 100 \text{ W}$ ,  $v = 900 \text{ mm s}^{-1}$  and  $t = 60 \mu\text{m}$ ) improves  $M_s$  due to the bigger crystallites. In general, high  $h$

reduces the volumetric energy input to powder, increasing the amorphous content resulting from high cooling rate. Also, it is clear that  $h$  and  $v$  are the controlling parameters for saturation magnetization as the combination of  $h = 30 \mu\text{m}$  and  $v = 1,000 \text{ mm s}^{-1}$  gives the higher saturation magnetization at different layer thicknesses and lower powers. The reason for this could be that those parameters provide sufficient undercooling so that smaller crystallites spread in amorphous matrix at a smaller distance, which improves exchange interaction among them and increases  $M_s$ . The thermal evolution in the LPBF process is complex and it is hard to comprehend what happens thermally during the process as a variety of process parameters influence its thermal development.

In this study, coercivity ( $H_c$ ) depends on the microstructural features such as defects (pores and cracks), amorphous content, and crystallite size. As mentioned before,  $H_c$  is reduced by increasing the amount of amorphous phase or by increasing the crystallite size above 500 nm, while decreasing the magneto-crystalline anisotropy. However, the crystallite size in this study (50–1,000 nm) (Figure 6a, 7a, 8a, 9a) is mostly in the constant-coercivity region ( $D: 100\text{--}500 \text{ nm}$ ,  $H_c: \approx 2 \text{ kA m}^{-1}$ [24]), which means varying the crystallite size in this range does not affect the coercivity. Additionally, the red regions (high bulk density) in Figure 10 coincide with the yellow and green regions (low coercivity) in Figure 12 for the most part. Therefore, porosity

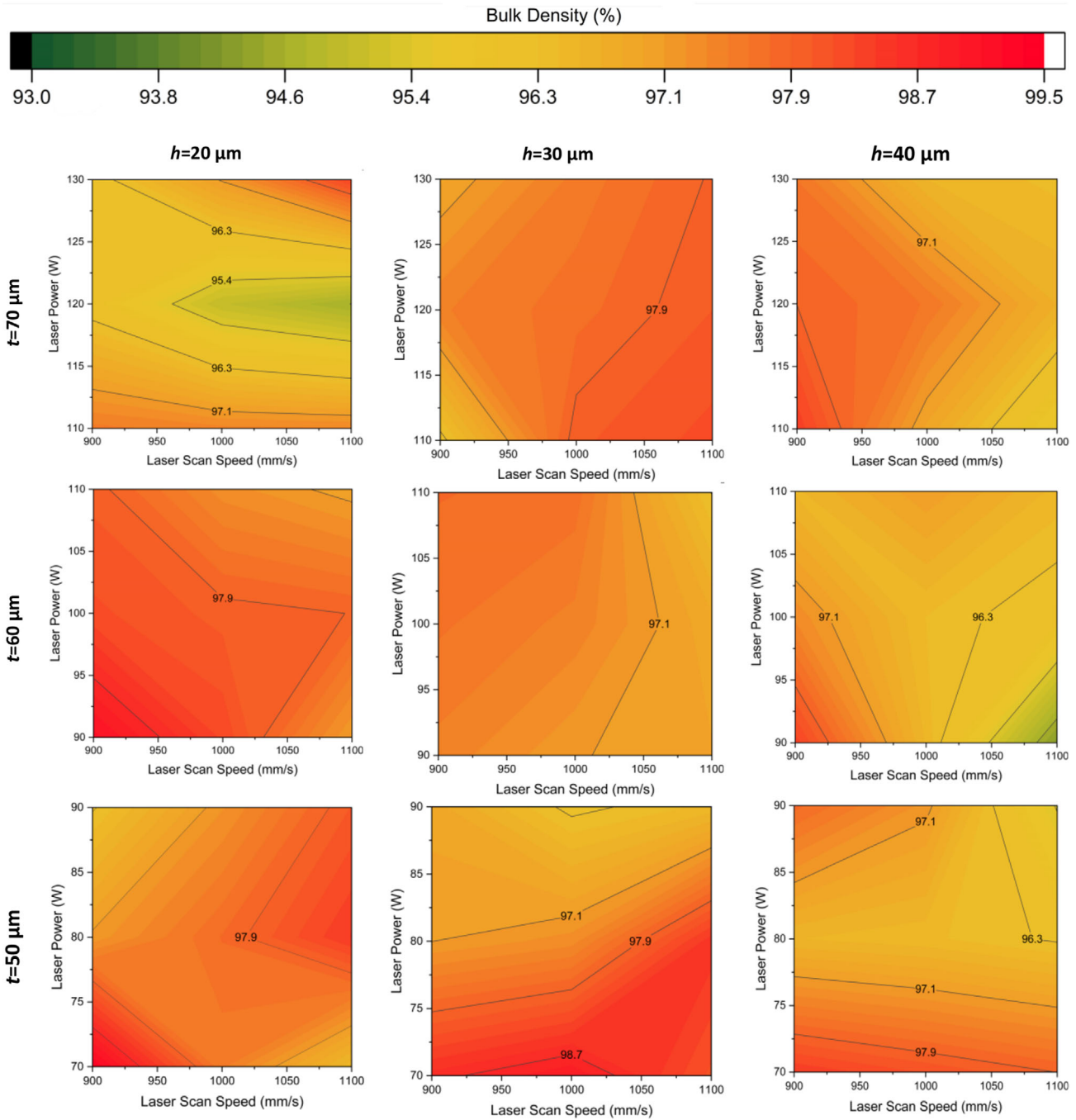


**Figure 10.** Color-mapped graphs showing bulk density variations as a function of laser power and laser scan speed at three different layer thicknesses ( $t$ ) and hatch spacing ( $h$ ) with the scale bar on top of the graphs.

level may impact the coercivity more than crystallite size in this work. Generally, it was observed that low  $P$  and  $v$  brought about low coercivity, which may result from the high bulk density observed at these parameters (Figure 12). Despite high bulk density and  $M_s$  achieved in this study, the coercivity is too high ( $1.35\text{--}2.72\text{ kA m}^{-1}$ ) for soft-magnetic materials applications. The coercivity needs to be reduced by lowering  $P$  and  $v$  or using different scanning strategy without compromising bulk density and saturation magnetization.

#### 4. Conclusion

FeSiBCrC BMGs were LPBF-processed with the help of different laser process parameters with the aim of obtaining high bulk density and excellent soft-magnetic properties. The results can be summarized as follows: 1) The thermal evolution (cooling rate and thermal gradient) during laser scanning influences the microstructure (the amorphous content and  $\alpha\text{-Fe}(\text{Si})$ ), which has a significant effect on the soft-magnetic properties. 2) The

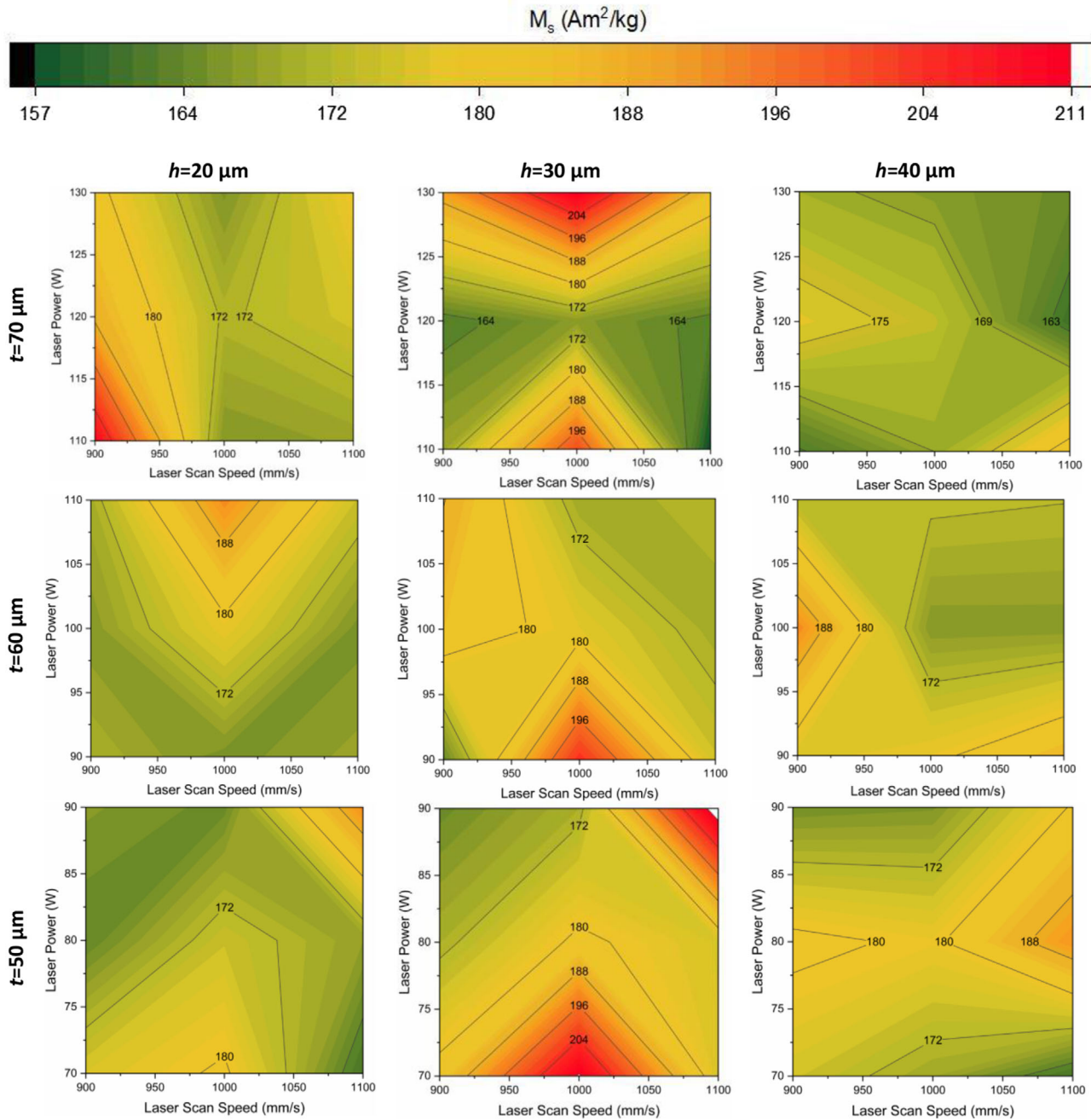


**Figure 11.** Color-mapped graphs showing saturation magnetization ( $M_s$ ) variations as a function of laser power and laser scan speed at three different layer thicknesses ( $t$ ) and hatch spacing ( $h$ ) with the scale bar on top of the graphs.

thermal modeling results indicated that the thermal gradient is primarily influenced by the laser power ( $P$ ). High thermal gradient and rapid cooling rates can only be achieved at low  $P$ . Furthermore, in addition to  $P$ , the laser scan speed ( $v$ ) also impacted the cooling rate and the depth of molten pools (MP), where higher  $v$  resulted in shallower MP depths and increased cooling rates. 3) A higher cooling rate and thermal gradient, achieved through low  $P$  and high  $v$ , encourage nucleation processes. In contrast, a lower cooling rate and thermal gradient,

obtained with high  $P$  and low  $v$ , accelerate grain growth, resulting in larger grain sizes rather than an increase in the number of grains. 4) In practical terms, a shorter hatch spacing can lead to reheating of the solidified part, particularly when considering the melt-pool size. This can result in in situ heat treatment, which is more significant for smaller component sizes. The study found that if the hatch spacing is too short, multiple reheating occurs, resulting in a lower cooling rate and promoting grain growth over nucleation in the microstructure. 5) Because of

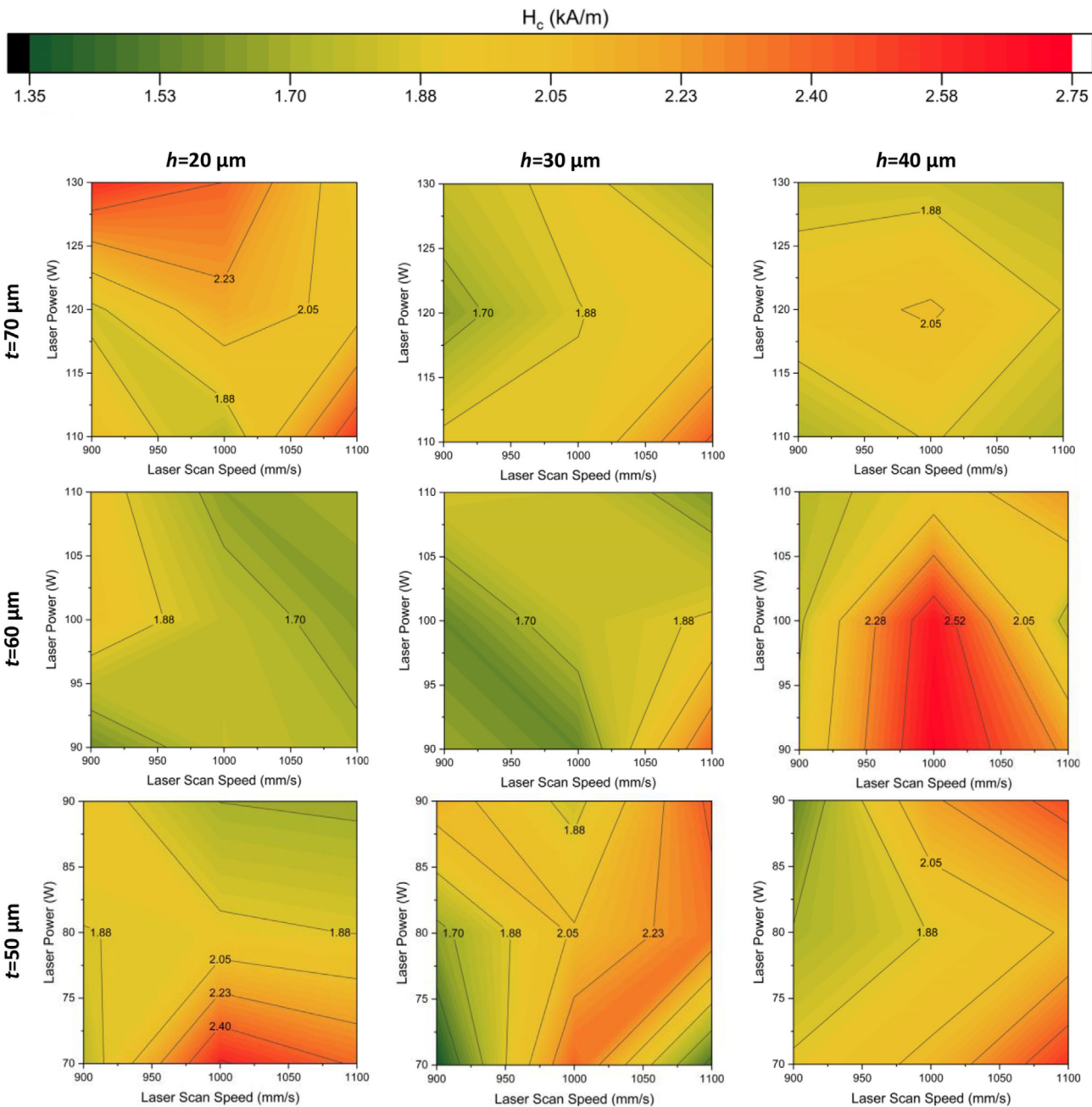


**Figure 12.** Color-mapped graphs showing coercivity ( $H_c$ ) variations as a function of laser power and laser scan speed at three different layer thicknesses ( $t$ ) and hatch spacing ( $h$ ) with the scale bar on top of the graphs.

the brittle nature of the BMGs, high thermal internal stresses tend to develop in the microstructures, leading to cracks. To prevent cracks formation, rapid cooling rate (high  $\nu$ ) and high energy input (high  $P$ ) should be avoided. Therefore, low  $P$  and  $\nu$  ought to be used along with low  $h$  and  $t$  to decrease cracks and porosity. 6) The controlling parameters for saturation magnetization are observed to be  $\nu$  and  $h$ .  $h$  of 30  $\mu\text{m}$  and  $\nu$  of 1,000  $\text{mm s}^{-1}$  give the highest  $M_s$  ( $\geq 200 \text{ Am}^2 \text{ kg}^{-1}$ ) at low laser power in this study. Those process parameters provided higher undercooling (nucleation rate is dominant) such that  $\alpha\text{-Fe}(\text{Si})$  phases decreased

in size and were distributed at a smaller distance, facilitating exchange interaction among them. 7) The crystallite size range examined (50–1,000 nm) mostly falls within the constant-coercivity region, indicating that variations in crystallite size within this range do not significantly affect the coercivity. The findings suggested that the porosity level might have a more significant impact on coercivity than crystallite size. It was generally observed that lower laser power ( $P$ ) and scan speed ( $\nu$ ) resulted in lower coercivity, which could be attributed to the higher bulk density achieved under these parameters.

## Appendix A The 3D-printed samples coded according to their laser process parameters

**Table A1.** The LPBF-processed samples by using layer thickness of 50  $\mu\text{m}$ , coded according to the process parameters (laser power ( $P$ ), laser scan speed ( $\nu$ ), hatch spacing ( $h$ )).

$h$ [ $\mu\text{m}$ ]	20			30			40		
$P$ ( $W$ )/ $\nu$ [ $\text{mm s}^{-1}$ ]	70	80	90	70	80	90	70	80	90
900	Sample 1	Sample 4	Sample 7	Sample 10	Sample 13	Sample 16	Sample 19	Sample 22	Sample 25
1,000	Sample 2	Sample 5	Sample 8	Sample 11	Sample 14	Sample 17	Sample 20	Sample 23	Sample 26
1,100	Sample 3	Sample 6	Sample 9	Sample 12	Sample 15	Sample 18	Sample 21	Sample 24	Sample 27

**Table A2.** The LPBF-processed samples by using layer thickness of 60  $\mu\text{m}$ , coded according to the process parameters (laser power ( $P$ ), laser scan speed ( $\nu$ ), hatch spacing ( $h$ )).

$h$ [ $\mu\text{m}$ ]	20			30			40		
$P$ ( $W$ )/ $\nu$ [ $\text{mm s}^{-1}$ ]	90	100	110	90	100	110	90	100	110
900	Sample 28	Sample 31	Sample 34	Sample 37	Sample 40	Sample 43	Sample 46	Sample 49	Sample 52
1,000	Sample 29	Sample 32	Sample 35	Sample 38	Sample 41	Sample 44	Sample 47	Sample 50	Sample 53
1,100	Sample 30	Sample 33	Sample 36	Sample 39	Sample 42	Sample 45	Sample 48	Sample 51	Sample 54

**Table A3.** The LPBF-processed samples by using layer thickness of 70  $\mu\text{m}$ , coded according to the process parameters (laser power ( $P$ ), laser scan speed ( $\nu$ ), hatch spacing ( $h$ )).

$h$ [ $\mu\text{m}$ ]	20			30			40		
$P$ ( $W$ )/ $\nu$ [ $\text{mm s}^{-1}$ ]	110	120	130	110	120	130	110	120	130
900	Sample 55	Sample 58	Sample 61	Sample 64	Sample 67	Sample 70	Sample 73	Sample 76	Sample 79
1,000	Sample 56	Sample 59	Sample 62	Sample 65	Sample 68	Sample 71	Sample 74	Sample 77	Sample 80
1,100	Sample 57	Sample 60	Sample 63	Sample 66	Sample 69	Sample 72	Sample 75	Sample 78	Sample 81

## Acknowledgements

The author would like to express very great appreciation to Dr. Richard Rowan-Robinson for kindly giving permission for the usage of the graph (Figure 1) that he created and to the Republic of Turkey Ministry of National Education for funding this project.

## Conflict of Interest

The authors declare no conflict of interest.

## Data Availability Statement

The data that support the findings of this study are available from the corresponding author upon reasonable request.

## Keywords

amorphous/nanocrystalline magnetic materials, laser additive manufacturing process optimization, laser powder bed fusion

Received: April 25, 2023

Revised: July 12, 2023

Published online:

- [1] V. Sufiarov, D. Erutin, A. Kantukov, E. Borisov, A. Popovic, D. Nazarov, *Materials* **2022**, *15*, 4121.
- [2] V. Chaudhary, S. Mantri, R. Ramanujan, R. Banerjee, *Prog. Mater. Sci.* **2020**, *114*, 100688.
- [3] Y. Nam, B. Koo, M. Chang, S. Yang, J. Yu, Y. Park, J. Jeong, *Mater. Lett.* **2020**, *261*, 127068.
- [4] L. Thorsson, M. Unosson, M. Perez-Prado, X. Jin, P. Tiberto, G. Barrera, B. Adam, N. Neuber, A. Ghavimi, M. Frey, R. Busch, I. Gallino, *Mater. Des.* **2022**, *215*, 110483.
- [5] T. Debroy, H. Wei, J. Zuback, T. Mukherjee, J. Elmer, J. Milewski, A. Beese, A. Wilson-Heid, A. De, W. Zhang, *Prog. Mater. Sci.* **2018**, *92*, 112.
- [6] H. Fayazfar, M. Salarian, A. Rogalsky, D. Sarker, P. Russo, V. Paserin, E. Toyserkani, *Mater. Des.* **2018**, *144*, 98.
- [7] C. Zhang, D. Ouyang, S. Pauly, L. Liu, *Mater. Sci. Eng. R: Rep.* **2021**, *145*, 100625.
- [8] H. Jung, S. Choi, K. Prashanth, M. Stoica, S. Scudino, S. Yi, U. Kuhn, D. Kim, K. Kim, J. Eckert, *Mater. Des.* **2015**, *86*, 703.

- [9] S. Alleg, R. Drablia, N. Fenineche, *J. Supercond. Novel Magn.* **2018**, *31*, 3565.
- [10] L. Zrodowski, B. Wysocki, R. Wroblewski, A. Kraczyńska, B. Adamczyk-Cieslak, J. Zduenk, P. Blyskun, J. Ferenc, M. Leonowicz, W. Swieszkowski, *J. Alloys Compd.* **2019**, *771*, 769.
- [11] S. Gao, X. Yan, C. Chang, E. Aubry, P. He, M. Liu, H. Liao, S. Fenineche, *Mater. Lett.* **2021**, *290*, 129469.
- [12] M. Ozden, N. Morley, *J. Alloys Compd.* **2023**, *960*, 170644.
- [13] T. Eagar, N. Tsai, in *the 64th Annual AWS Convention*, Philadelphia, **1983**.
- [14] A. Yazdani, G. Hohne, S. Mixture, O. Graeve, *PLoS One* **2020**, *15*, e0234774.
- [15] J. Konopka, *Options For Quantitative Analysis of Light Elements By SEM/EDS*, Thermo Fisher Scientific, Madison, WI, **2013**.
- [16] M. Wilard, M. Daniil, *Handbook of Magnetic Materials*, Vol. 21, Elsevier, Oxford, Great Britain **2013**, p. 173.
- [17] M. McHenry, D. Laughlin, *Phys. Metall.* **2014**, *19*, 1881.
- [18] T. Bitoh, A. Makino, A. Inoue, *Mater. Trans.* **2003**, *44* 2020.
- [19] K. Suzuki, R. Parsons, B. Zang, K. Onodera, H. Kishimoto, T. Shoji, A. Kato, *AIP Adv.* **2019**, *9*, 035311.
- [20] V. Tsepelev, Y. Starodubtsev, *Nanomaterials* **2021**, *11*, 108.
- [21] G. Herzer, *IEEE Trans. Magn.* **1990**, *26*, 1397.
- [22] G. Herzer, *Handbook of Magnetic Materials*, Vol. 10, Elsevier, Oxford, Great Britain **1997**, pp. 415–462, [https://doi.org/10.1016/S1567-2719\(97\)10007-5](https://doi.org/10.1016/S1567-2719(97)10007-5).
- [23] S. Flohrer, G. Herzer, *J. Magn. Magn. Mater.* **2010**, *322*, 1511.
- [24] G. Herzer, *Acta Mater.* **2013**, *61*, 718.
- [25] M. Celikbilek, A. Ersundu, S. Aydin, *Advances in Crystallization Processes*, Intech, Istanbul, Turkey **2012**, pp. 127–162.
- [26] N. Prasad, K. Varma, *J. Am. Ceram. Soc.* **2005**, *88* 357.
- [27] R. Li, J. Liu, Y. Shi, L. Wang, W. Jiang, *Int. J. Adv. Manuf. Technol.* **2012**, *59*, 1025.
- [28] M. Narwam, K. Al-Rubaie, M. Elbestawi, *Materials* **2012**, *12*, 2284.
- [29] Q. Jiang, P. Zhang, J. Tan, Z. Yu, Y. Tian, S. Ma, D. Wu, *J. Alloys Compd.* **2022**, *894*, 162525.